



Article

Influence of Ni and Nb Addition in TiVCr-Based High Entropy Alloys for Room-Temperature Hydrogen Storage

Srilakshmi Jeyaraman ^{1,2,3}, Dmitri L. Danilov ^{4,5,*}, Peter H. L. Notten ^{4,5}, Udaya Bhaskar Reddy Ragula ^{1,2,3}, Vaira Vignesh Ramalingam ⁶ and Thirugnasambandam G. Manivasagam ^{1,2,3,*}

- Department of Chemical Engineering and Materials Science, Amrita School of Engineering, Amrita Vishwa Vidyapeetham, Coimbatore 641112, India; j_srilakshmi@cb.amrita.edu (S.J.); u_bhaskarreddy@cb.amrita.edu (U.B.R.R.)
- ² Centre of Excellence in Advanced Materials and Green Technologies (CoE-AMGT), Amrita School of Engineering, Amrita Vishwa Vidyapeetham, Coimbatore 641112, India
- ³ Amrita Center for Energy Technology and Innovation (CoE-AMGT), Amrita School of Engineering, Amrita Vishwa Vidyapeetham, Coimbatore 641112, India
- Fundamental Electrochemistry (IET-1), Forschungszentrum Jülich, D-52425 Jülich, Germany; p.h.l.notten@fz-juelich.de
- Electrical Engineering Department, Eindhoven University of Technology, 5600 MB Eindhoven, The Netherlands
- Department of Mechanical Engineering, Amrita School of Engineering, Amrita Vishwa Vidyapeetham, Coimbatore 641112, India; r_vairavignesh@cb.amrita.edu
- * Correspondence: d.danilov@fz-juelich.de (D.L.D.); gm_thiru@cb.amrita.edu (T.G.M.)

Abstract

TiVCr-based alloys are well-explored body-centered cubic (BCC) materials for hydrogen storage applications that can potentially store higher amounts of hydrogen at moderate temperatures. The challenge remains in optimizing the alloy-hydrogen stability, and several transition elements have been found to support the reduction in the hydride stability. In this study, Ni and Nb transition elements were incorporated into the TiVCr alloy system to thoroughly understand their influence on the (de)hydrogenation kinetics and thermodynamic properties. Three different compositions, (TiVCr)₉₅Ni₅, (TiVCr)₉₀ Ni₁₀, and (TiVCr)₉₅Ni₅Nb₅, were prepared via arc melting. The as-prepared samples showed the formation of a dual-phase BCC solid solution and secondary phase precipitates. The samples were characterized using hydrogen sorption studies. Among the studied compositions, (TiVCr)₉₀Ni₁₀ exhibited the highest hydrogen absorption capacity of 3 wt%, whereas both (TiVCr)₉₅Ni₅ and (TiVCr)₉₀Ni₅Nb₅ absorbed up to 2.5 wt% hydrogen. The kinetics of (de)hydrogenation were modeled using the JMAK and 3D Jander diffusion models. The kinetics results showed that the presence of Ni improved hydrogen adsorption at the interface level, whereas Nb substitution enhanced diffusion and hydrogen release at room temperature. Thus, the addition of Ni and Nb to Ti-V-Cr-based high-entropy alloys significantly improved the hydrogen absorption and desorption properties at room temperature for gas-phase hydrogen storage.

Keywords: hydrogen storage; TiVCrNi alloy; TiVCrNiNb alloy; BCC solid solution; secondary phase; kinetic modeling

check for updates

Academic Editor: Roger Gläser

Received: 16 May 2025 Revised: 30 June 2025 Accepted: 6 July 2025 Published: 23 July 2025

Citation: Jeyaraman, S.; Danilov, D.L.; Notten, P.H.L.; Ragula, U.B.R.; Ramalingam, V.V.; Manivasagam, T.G. Influence of Ni and Nb Addition in TiVCr-Based High Entropy Alloys for Room-Temperature Hydrogen Storage. *Energies* **2025**, *18*, 3920. https://doi.org/10.3390/en18153920

Copyright: © 2025 by the authors. Licensee MDPI, Basel, Switzerland. This article is an open access article distributed under the terms and conditions of the Creative Commons Attribution (CC BY) license (https://creativecommons.org/licenses/by/4.0/).

1. Introduction

Globally, the rise in greenhouse gas emissions is a concerning and challenging threat to human survival. In particular, approximately 59% of greenhouse gas emissions (GHGs) originate from the transportation sector [1]. Efforts to minimize carbon emissions through

Energies **2025**, *18*, 3920 2 of 19

the use of renewable resources have increased. In particular, hydrogen energy is considered a viable alternative approach for achieving net-zero emissions in mobile and stationary applications [2]. Conversely, the scaling up of hydrogen production and storage is emerging as a key research focus for developing greener energy systems [3–5]. Metal hydrides (MHs) are solid-state materials that can store hydrogen safely and compactly, providing better reversibility with high gravimetric and volumetric energy densities [6,7]. High-entropy alloys (HEA) have recently gained significant attention as potential hydrogen storage materials. HEA have more than five different constituent elements at equal or non-equal non-equiatomic ratios, providing high selectivity of elements and tunability of the compositions. These variations significantly change the hydrogen kinetic and thermodynamic performances [8–15]. Some challenges that are common for commercial metal hydrides (typically binary or multicomponent alloy systems) are found to show limited influence on altering the compositional parameters that are important for tuning hydride stability or improving kinetic properties at moderate temperatures [16–20].

TiV-based alloys can store large amounts of hydrogen (>3 wt%), providing a greater advantage in hydrogen absorption at room temperature [21,22]. Some popular TiV(M) BCC-based alloys are doped with elements such as Cr, Zr, Nb, and Mn, which have been found to exhibit high gravimetric hydrogen capacities at moderate temperatures [23–33]. The addition of these (non-)transition elements enhances the kinetic and thermodynamic properties while also helping to reduce the vanadium usage and overall material cost. Some practical challenges involved in BCC structures are (i) poor hydrogen reversibility under ambient conditions due to the formation of a monohydride phase, (ii) requires activation, and (iii) hysteresis loss during (de)absorption cycles, and (iv) requires high temperature for hydrogen desorption (>300 °C) [34]. Compared to commercially available intermetallic compounds such as (AB, AB₂, and AB₅), which can typically store only 1–2 wt% of hydrogen, the BCC structure can absorb large amounts of hydrogen at room temperature, which is essential for light-duty hydrogen storage applications [35,36].

TiVCr-based alloys are considered promising hydrogen storage materials because the addition of Cr helps to tune the plateau pressure and reduce the oxidation effects of V and Ti [37,38]. At room temperature, it can form a single-phase BCC solid solution with a high hydrogen content (3–4 wt% H2). However, TiVCr presents a low plateau pressure range during the (de)hydriding process at room temperature. Thus, from a thermodynamic perspective, higher temperatures (~300 °C) are required for the complete hydrogen desorption process [32,39,40]. Several reports have stated that the plateau pressure can be tuned by varying the compositional range substitution of non-hydriding elements such as Fe, Al, Ni, Mn, and Nb, which significantly improve the kinetics and thermodynamic properties during the (de)hydriding process [28,30,31,41]. According to Vegard's law, the lattice parameter has a direct effect on the stability of the hydride [27,42,43], leading to a shift in the equilibrium plateau pressure range. That, in turn, influences the desorption onset temperature and overall hydrogen storage capacity. An appropriate plateau pressure near atmospheric pressure and moderate temperature (<100 °C) is essential for light-duty vehicular applications. Thus, TiVCr-based alloys have the potential to meet the Department of Energy (DoE) criteria because of their higher hydrogen storage capacity and tunable properties to reduce the stability of hydrides by the addition of non-transition elements [44,45].

Chao et al. investigated the relationship between the lattice parameter and Ti/Cr ratio in the TiVCr alloy system. Altering the titanium-to-chromium ratio to a value higher than 0.75 significantly affected the plateau pressure range [46]. The Seemita et al. group studied a series of Ti-V-Cr-based quaternary alloy systems. It has been reported that for the $Ti_{2-x}CrVM_x$ (M=Fe, Co, Ni) alloy system, substituting Ti with non-transition

Energies **2025**, 18, 3920 3 of 19

elements leads to improved hydriding performance. For instance, the addition of Ni improved the kinetic performance, achieving a hydrogen storage capacity of 3.9 wt% at room temperature. In another report, replacing Ti with Al in the Ti₂VCr system increased the plateau pressure to 0.1 bar at room temperature. When the Al concentration is increased from 5 wt% to 10 wt%, a decrease in the hydrogen storage capacity and kinetics properties is observed [47,48]. Similarly, Wang et al. reported the role of Fe in a V-rich BCC alloy; with results showing enhanced cyclic stability and hydrogen storage capacity of 3.8 wt% H₂. The plateau pressure increased when the Fe concentration was up to 3 wt% for V_{75} -Ti-Cr-Fe_y (Ti/Cr = 0.9, y = 0-6) at room temperature, maintaining good reversibility. Kumar et al. showed that the Ti₂CrV alloy exhibited good reversibility up to 3.5 wt% at room temperature [49]. Thus, several reports have proven that the addition of transition and non-transition metals to TiVCr alloys significantly impacts the hydrogen sorption properties, with some direct influences on the thermodynamic properties. Few reports have presented TiVCr alloys with composites such as LaNi₅, TiMn₂, ZrFe_{1.8}V_{0.2}, and other rare-earth elements. The presence of secondary phases inhibited the storage capacity but increased the equilibrium plateau pressure [50–52]. Lave-phase-related BCC alloys are easily achieved by substituting non-transition metals. Some reports also show that the presence of the lave phase in BCC, multicomponent, and high-entropy alloys significantly enhances the hydrogen kinetics and decreases the hydride stability [53].

Similarly, Zhu investigated a complex doping strategy using a high-entropy alloy in the TiVCr system [54]. The addition of HEA showed a synergistic effect in improving hydrogen storage performance. It was effectively able to release 1.73 wt% of hydrogen at 1 bar pressure (70 °C) for TiCr_{1.0}V_{0.7}(NbFeCoNiMn)_{0.2} with a minor presence of C14 secondary phase. Zhu et al. demonstrated that the substitution of Nb in Ti-V-Cr alloys has a significant impact on cyclic durability [30]. TiVCrNb is another well-explored multicomponent BCC high-entropy alloy capable of absorbing hydrogen at a high capacity of 2 H/M. The ratio of Cr and the valence electron concentration plays a crucial role in determining its thermodynamic properties [55,56]. Ankita et al. conducted a detailed comparative analysis of the bulk-level synthesis of BCC alloys using arc melting (AM) and induction melting (IM) methods to characterize hydrogen storage performance. The 52Ti-12V-36Cr + 4 wt% Zr alloy was synthesized in bulk using both AM and IM techniques. The synthesized alloy consisted of BCC and secondary lave phases. The sample prepared via the AM method stored 3.5 wt% hydrogen at room temperature. In the IM method, traces of TiC contamination were detected during the melting process in the graphite crucible, which adversely affected the hydriding kinetics and cyclic properties, resulting in a storage capacity of 2.9 wt%. The authors have highlighted that the production and commercial scaling of TiVCr present significant challenges, primarily due to the impact of the synthesis method on storage capacity [57].

Based on the above discussion and extensive work on tuning the properties of TiV-based alloys, significant efforts have been made to explore suitable non-hydriding elements that can enhance the kinetic properties and reduce the stability of the hydride. The addition of Ni to TiVCr-based alloys has been reported to be beneficial in destabilizing the alloy-hydrogen stability, also leading to the formation of secondary phases that provide pathways for hydrogen uptake and release [58–61]. In addition, the addition of Nb to TiVCr was found to improve its cyclic stability [30,62]. To further explore the contribution of the addition of Ni and Nb to TiVCr base alloys, in this study, quaternary and quinary alloys, $(\text{TiVCr})_x \text{Ni}_{1-x}$ and $(\text{TiVCr})_x \text{Ni}_{1-x} \text{Nb}_5$ (x = 0.90, 0.95), were prepared via the arc melting method. The hydrogen storage properties were investigated through kinetic measurements conducted at various temperatures. Furthermore, kinetic modeling was performed to comprehend how the addition of Ni and Nb to the base matrix of the TiVCr alloy affects the

Energies **2025**, 18, 3920 4 of 19

hydrogen storage capabilities at different temperatures. This study aims to (i) understand the role of Ni in TiVCr, (ii) understand the role of Nb in TiVCrNi, and (iii) evaluate the consequent contribution of Nb to the effective hydrogen storage capacity.

2. Experimental

2.1. Sample Preparation

Ti rod (Thermo Scientific, Walham, MA, USA, 99.99% purity), Cr pieces (Thermo Scientific, 99.99% purity), Vanadium sheets (Thermo Fisher, 99.7% purity), Nb pieces (Thermo Scientific, 99.99% purity), and Ni pieces (Alfa Aesar, Haverhill, MA, USA 99.8%) were weighed based on the required composition proportions, as shown in Table 1. Three compositions of TiVCr-based quaternary and quinary high-entropy alloys were synthesized using the vacuum arc melting method. The stoichiometries of the compositions are $(\text{TiVCr})_x \text{Ni}_{1-x}$ and $(\text{TiVCr})_x \text{Ni}_{1-x} \text{Nb}_5$ (x = 0.90, 0.95), i.e., $(\text{TiVCr})_95 \text{Ni}_5$, $(\text{TiVCr})_90 \text{Ni}_{10}$, and $(\text{TiVCr})_95 \text{Ni}_5 \text{Nb}_5$, respectively. Before melting, the arc chamber was continuously purged with ultra-high-purity argon gas, and the Ti getter was melted to trap the residual oxygen gas. All three compositions were melted four times to maintain the homogeneity of the sample. The as-synthesized alloy was mechanically crushed under hydraulic pressure (load range 40–60 kN) and further characterized for its structural and hydrogen storage properties.

Table 1. HEA calculated the parameter values.

Composition	ΔS_{mix}	ΔH_{mix}	δ	Ω	VEC	ΔH_{∞}	$\overset{-}{\Delta H_f^\circ}$
(TiVCr) ₉₅ Ni ₅	10.33	-8.16	6.68	2.62	5.24	-17.51	-37.44
$(TiVCr)_{90}Ni_{10}$	10.92	-11.16	6.69	2.02	5.50	-16.1	-35.70
$(TiVCr)_{90}Ni_5Nb_5$	11.50	-8.22	6.65	2.96	5.25	-18.5	-37.45

Units: ΔS (J/K·mol), δ (%), ΔH , $\overline{\Delta H_{\infty}}$ and $\overline{\Delta H_{f}^{\circ}}$ (KJ/mol).

2.2. Characterization Method

The as-synthesized high entropy alloys were characterized by the X-ray diffraction technique at a scan rate 1°/min and a scan range of 10-90 degrees using a Rigaku X-ray diffractometer with a tube voltage of 40 kV and current of 30 mA (Cu kα radiation). The hydrogenation properties were determined using a Sievert-type apparatus (Hydata PCT pro 2000, Setaram, Caluire, France). Kinetic measurements were taken at three different temperatures (20, 100, and 200 °C) by applying a pressure of 30 bar. Thermal analysis was performed for all three compositions after fully hydriding the alloys to measure the complete hydrogen desorption temperature. The hydrided samples were carefully removed from the PCT pro instrument, and the sample holders were dismantled inside an argon-filled glove box to carry out chemisorption measurements using temperatureprogrammed desorption (H₂-TPD) in a Quantachrome Autosorb iQ-C-XR instrument (Anton Paar, Gurugram, India). Approximately 120 mg of the hydrided sample was loaded into the quartz sample holder and purged with ultra-high-purity helium gas at a flow rate of 300 μ L/min (1 bar). The heating rate was 5 °C/min, measured up to 500 °C. The properties of the hydrogen-desorbed alloys were measured using a thermal conductivity detector (TCD). After complete desorption, the samples were characterized using XRD to understand the phase stability of the alloy. The microstructures of the samples were examined using field-emission scanning electron microscopy (Gemini 300, Carl Zeiss, Bangalore, India).

The formation of a single-phase high-entropy alloy is based on calculating criteria such as configurational entropy (ΔS), atomic size difference (δ), enthalpy of alloy formation

Energies **2025**, 18, 3920 5 of 19

 (ΔH) , thermodynamic parameter (Ω) , and valence electron count (VEC). The following equations theoretically describe the formation of HEA and their expected phases.

Entropy of mixing (ΔS)

$$\Delta S_{mix} = -R \sum_{i=1, j\neq j}^{n} c_i lnc_i,$$

where R is the gas constant and c_i is the atomic percent.

Atomic size difference (δ)

$$\delta = 100\sqrt{\sum_{i=1}^{n} c_i \left(1 - \frac{r_i}{\overline{r}}\right)^2}, \delta \le 6.6,$$

where $\bar{r} = \sum_{i=1}^{n} c_i r_i$, $c_i r_i$ atomic percent and atomic radius of the i^{th} element.

Thermodynamic parameter (Ω)

$$\Omega = rac{T_m \Delta S_{mix}}{|\Delta H_{mix}|}, \Omega > 1$$

Enthalpy of alloy formation (ΔH)

$$\Delta H_{mix} = \sum_{i=1, i\neq j}^{n} \Omega_{ij} c_i c_j,$$

where $\Omega_{ij} = 4\Delta H_{ij}^{AB}$, +3.2kJ/mol $\leq \Delta H_{mix} \geq -12.6$ kJ/mol. The enthalpy of mixing of binary alloy AB (Δ H) are based on the Miedema macroscopic model [63].

Valence electron configuration (VEC)

$$VEC = \sum_{i=1}^{n} c_i (VEC)_i,$$

where VEC < 6.87 tends to form BCC whereas VEC > 8 forms FCC solid solution [64].

In this work, $\overline{\Delta H_{\infty}}$ and $\overline{\Delta H_f^{\circ}}$ are calculated using the following equations from reference [65], where $(\Delta H_{\infty})_i$ is the enthalpy of hydrogen solution at infinite dilution and $(\Delta H_f^{\circ})_i$ is the standard enthalpy of formation of element i. The values are referred from [66]. The calculated values are shown in Table 1.

$$\overline{\Delta H_{\infty}} = \sum_{i=1}^{N} \{ c_i (\Delta H_{\infty})_i \}$$

$$\overline{\Delta H_f^{\circ}} = \sum_{i=1}^{N} \left\{ c_i \left(\Delta H_f^{\circ} \right)_i \right\}$$

3. Results and Discussion

3.1. Structural Analysis

The XRD patterns of $(\text{TiVCr})_{95}\text{Ni}_5$, $(\text{TiVCr})_{90}\text{Ni}_{10}$, and $(\text{TiVCr})_{95}\text{Ni}_5\text{Nb}_5$ for the assynthesized, hydrogenated, and dehydrogenated samples are compared and shown in Figure 1a–c. All three compositions exhibited the existence of dual phases consisting of BCC and secondary phases. Quantitative phase analysis was performed using Xpert Highscore Plus (Malvern Panalytical B.V., Almelo, The Netherlands). Table 2 shows the structural parameters of the as-synthesized alloys. The BCC lattice parameter for $(\text{TiVCr})_{95}\text{Ni}_5$, $(\text{TiVCr})_{90}\text{Ni}_{10}$ was found to decrease slightly from 3.048 to 3.042 Å, and this is mainly due

Energies **2025**, 18, 3920 6 of 19

to the addition of small atom Ni (1.25 Å) [59,67]. Although the addition of Nb (1.48 Å) is expected to increase the lattice value, a decrease in the lattice parameter is observed. This reduction in the lattice parameter for (TiVCr)₉₅Ni₅Nb₅ correlates well with the calculated atomic size difference (δ) values provided in Table 1, which also show a slight decrease. That may cause a lattice distortion effect due to atomic mismatch, which is generally observed in HEA. For (TiVCr)₉₅Ni₅ and (TiVCr)₉₀Ni₁₀, the phase fraction of the BCC matrix decreased from 82.2% to 52.8%, attributed to an increase in secondary phase formation. The observed secondary phase is Cr_{0.8}Ni_{0.2} substitutional solid-solution phase (BCC). The increase in the phase fraction of the secondary phase for the (TiVCr)₉₀Ni₁₀ composition also matched with an increase in Δ H from -8.16 to -11.16 kJ/mol (Table 1). For (TiVCr)₉₅Ni₅Nb₅, a vanadium-dominant BCC solid solution and secondary phase belong to the face-centered cubic C15 (MgCu₂) lave phase (MgCu₂, S.G: Fd 3 m) with total volume fractions of 89.6% and 10.4%, respectively [68].

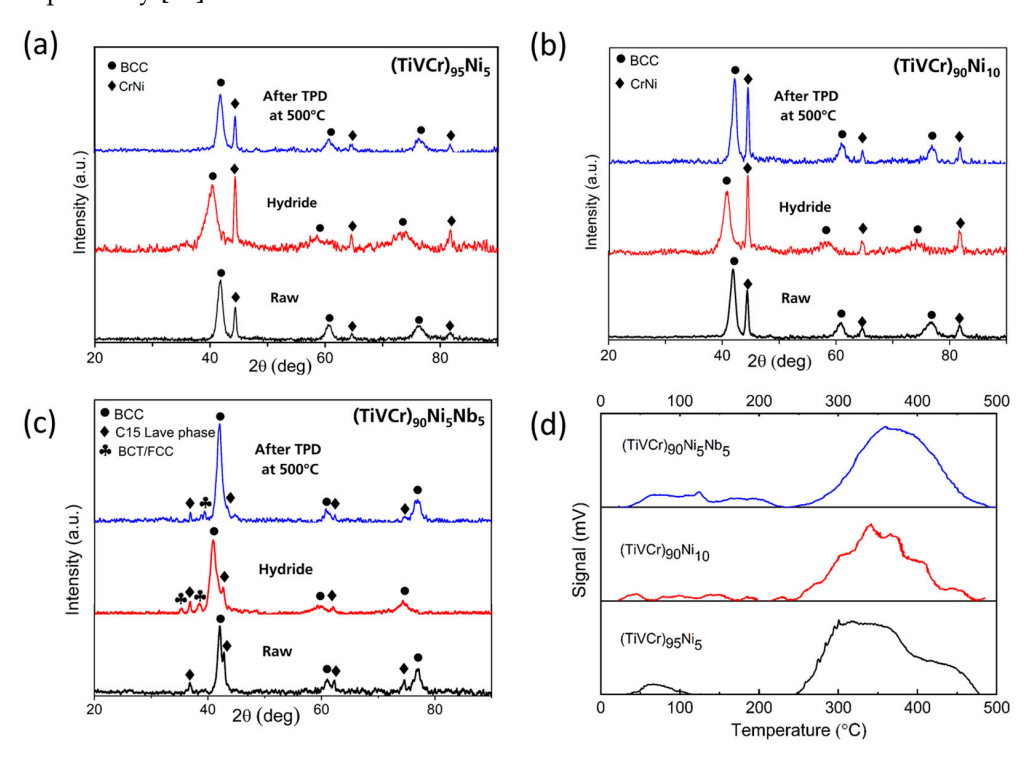


Figure 1. XRD diffraction pattern for $(\text{TiVCr})_{95}\text{Ni}_5$ (a), $(\text{TiVCr})_{90}\text{Ni}_{10}$ (b), and $(\text{TiVCr})_{90}\text{Ni}_5\text{Nb}_5$ (c) compositions for as-synthesized alloy, fully hydrogenated at 30 bar, and fully dehydrided after TPD measurement and (d) results of temperature-programmed desorption (H₂-TPD).

In the case of the hydrided sample, a peak shift in the BCC phase was observed for $(\text{TiVCr})_{95}\text{Ni}_5$, $(\text{TiVCr})_{90}\text{Ni}_{10}$, and $(\text{TiVCr})_{95}\text{Ni}_5\text{Nb}_5$, attributed to the absorption of hydrogen in the BCC lattice, causing volume expansion. Table 2 shows the lattice parameter details of the hydride sample measured after several repeated cyclic studies. The volume expansion percentages in the BCC phase upon hydrogenation were observed to be 11.17%, 10.09%, and 10.59% for $(\text{TiVCr})_{95}\text{Ni}_5$, $(\text{TiVCr})_{90}\text{Ni}_{10}$, and $(\text{TiVCr})_{95}\text{Ni}_5\text{Nb}_5$, respectively. The secondary phase exhibited no peak shift for the as-synthesized material. However, a slight change was observed in the hydrided phase, which may be attributed to the repeated cyclic effect that induces pulverization. For $(\text{TiVCr})_{95}\text{Ni}_5\text{Nb}_5$, in addition to the presence of a secondary phase, small traces of the BCT/FCC hydride phase were observed for the hydrided sample at $2\theta = 35.3$ and 38.5° [68]. Figure 1a–c shows the diffraction pattern of the fully desorbed state of the alloy measured after performing temperature-programmed desorption (TPD) at a temperature of 500 °C. All compositions retained their original phases, which were

Energies **2025**, 18, 3920 7 of 19

present in the as-synthesized samples, and the XRD reflections did not exhibit any peak shifts, confirming the structural stability of the alloy.

Table 2. Lattice parameter evaluated by XRD analysis for as-synthesized and hydrided alloy for
(TiVCr) ₉₅ Ni ₅ , (TiVCr) ₉₀ Ni ₁₀ , and (TiVCr) ₉₅ Ni ₅ Nb ₅ compositions.

	As-Synthesized				Hydride			
Composition	Phase	Phase Fraction (%)	Lattice Parameter (Å)	* Cell Volume (ų)	Phase	Lattice Parameter (Å)	* Cell Volume (ų)	
(TiVCr) ₉₅ Ni ₅	BCC	82.2	a = 3.048	28.31	BCC Hydride	a = 3.159	31.52	
	Secondary BCC	17.8	a = 2.881	23.91	Secondary BCC	a = 2.884	23.98	
(TiVCr) ₉₀ Ni ₁₀	BCC	52.8	a = 3.042	28.14	BCC Hydride	a = 3.141	30.98	
	Secondary BCC	47.2	a = 2.880	23.88	Secondary BCC	a = 2.898	24.33	
(TiVCr) ₉₅ Ni ₅ Nb ₅	BCC	89.6	a = 3.038	28.04	BCC Hydride	a = 3.142	31.01	
	C15 Lave phase	10.4	a = 6.951	335.8	C15 Lave phase	a = 6.992	341.8	

^{*} Cell volume is the unit cell volume in $Å^3$.

3.2. Microstructural Analysis

Figure 2 shows backscattered electron (BSE) images of all three compositions (a–c) depicting arc-melted alloys and (d–f) hydrided samples for $(\text{TiVCr})_{95}\text{Ni}_5$, $(\text{TiVCr})_{90}\text{Ni}_{10}$, and $(\text{TiVCr})_{90}\text{Ni}_5\text{Nb}_5$ compositions. The as-synthesized alloy comprised dark and light regions, attributed to the presence of two-phase regions, BCC (dark phase) + secondary phase (light phase). In the case of the Nb-substituted quinary alloy from the BSE result (Figure 2c), the as-cast alloy also presented BCC and secondary phases. Figure 2d–f shows the BSE images of the hydrogenated samples for all three compositions. The pulverization of the alloy during the hydriding process was observed in all three compositions. This type of crack or break is generally observed during repeated cyclic studies of metal hydride systems [69,70].

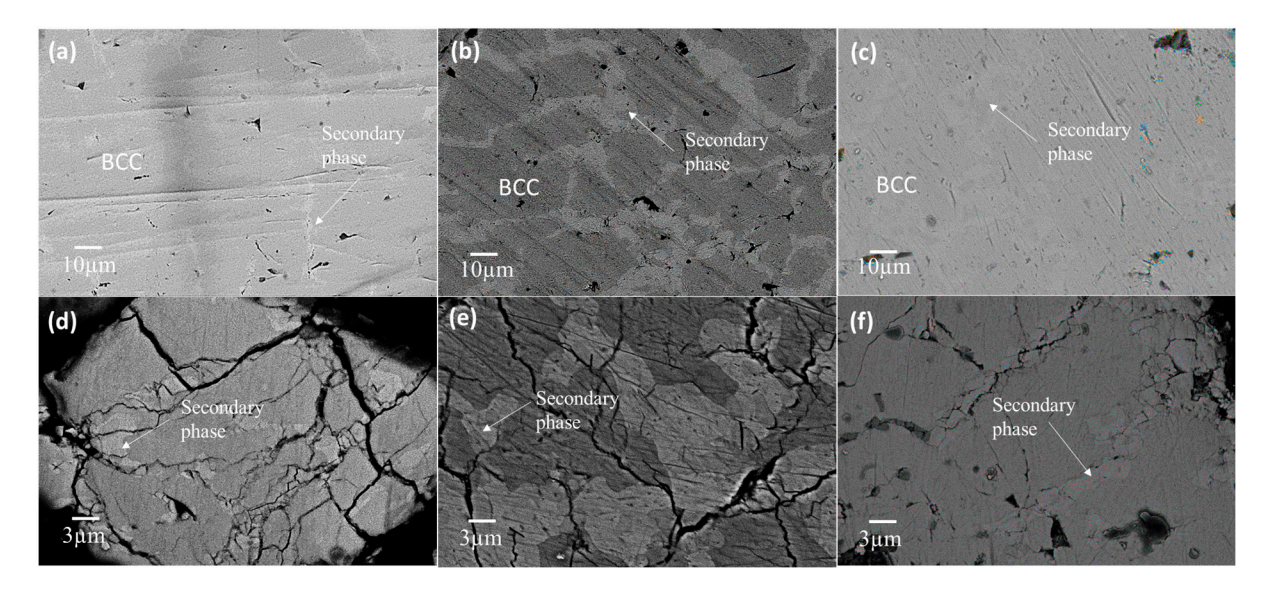


Figure 2. BSE images of as-cast alloy (**a–c**) and hydride phase of $(TiVCr)_{95}Ni_5$, $(TiVCr)_{90}Ni_{10}$, and $(TiVCr)_{90}Ni_5Nb_5$ compositions (**d–f**).

3.3. Kinetics Measurement

Kinetic measurements were performed at different temperatures (20, 100, and 200 °C). Initially, all the samples were measured at room temperature and under a constant pressure of 30 bars. Before every new kinetic absorption measurement, the alloy was heated up to 300 °C and evacuated under vacuum (10^{-2} bar) for complete hydrogen desorption. The results of the absorption–desorption kinetics for all three compositions are shown in Figure 3 and Table 3. (TiVCr)95Ni5, (TiVCr)90Ni10, and (TiVCr)90Ni5Nb5 compositions

Energies **2025**, *18*, 3920 8 of 19

showed hydrogen uptake at room temperature. It is observed for all three compositions that the hydrogen absorption capacity decreases with respect to an increase in temperature (>100 °C). Similar results on the temperature-independent decrease in hydrogen absorption have also been observed in a few previous studies. This decrease in storage capacity can be attributed to two possible reasons: (i) the hydrogenation process is exothermic, and both hydrogenation and dehydrogenation reactions compete with each other, leading to a decrease in the storage capacity at high temperatures, and (ii) an increase in the equilibrium pressure as a result of an increase in temperature [71–74]. The total absorption capacities of $(\text{TiVCr})_{95}\text{Ni}_5$ and $(\text{TiVCr})_{90}\text{Ni}_5\text{Nb}_5$ at room temperature were similar at 2.5 wt% H₂, whereas that of $(\text{TiVCr})_{90}\text{Ni}_{10}$ showed a slight increase in capacity value up to 3 wt% H₂. The total time to complete the hydrogenation process was 45, 65, and 35 min for $(\text{TiVCr})_{95}\text{Ni}_5$, $(\text{TiVCr})_{90}\text{Ni}_{10}$, and $(\text{TiVCr})_{90}\text{Ni}_5\text{Nb}_5$, respectively, at room temperature. Thus, the concentration of Ni and the addition of Nb to the (TiVCr) HEA significantly impacted the total capacity and (de)hydrogenation rate.

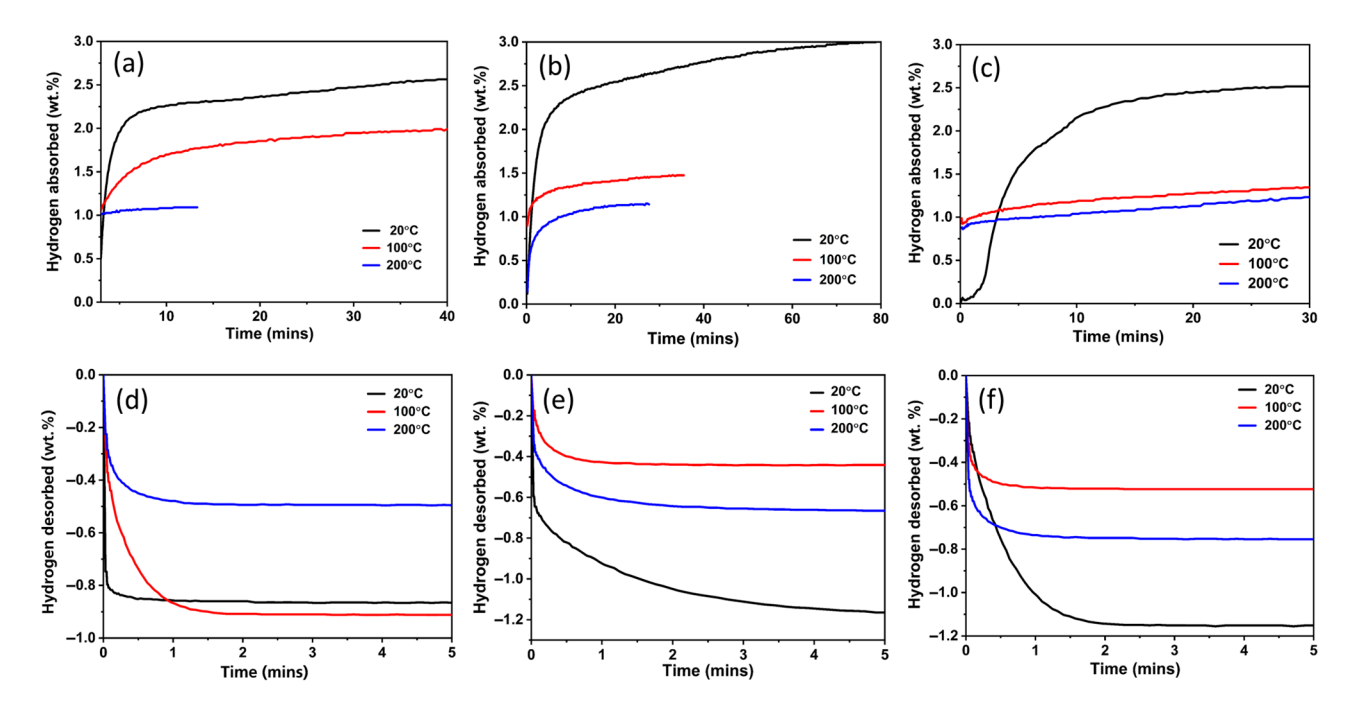


Figure 3. Hydrogen absorption/desorption kinetic profile of (TiVCr) $_{95}$ Ni $_{5}$ (a,d), (TiVCr) $_{90}$ Ni $_{10}$ (b,e), and (TiVCr) $_{90}$ Ni $_{5}$ Nb $_{5}$ (c,f) are measured at temperatures 20 °C, 100 °C, and 200 °C. For the desorption measurements, the pressure was set to 0.02 bar.

Table 3. Hydrogenation absorption (abs) and desorption (des) behavior at different temperatures. Units are in wt%.

Commonition	20 °C		100	°C	200 °C	
Composition	abs	des	abs	des	abs	des
(TiVCr) ₉₅ Ni ₅	2.50	0.86	2.00	0.91	1.09	0.49
(TiVCr) ₉₀ Ni ₁₀	3.00	1.20	1.47	0.44	1.14	0.68
(TiVCr) ₉₀ Ni ₅ Nb ₅	2.50	1.15	1.35	0.53	1.22	0.75

Several reports have indicated that the existence of the lave phase, which is a type of intermetallic phase, plays a significant role in promoting hydrogen diffusion across grain boundaries [58,72,75–78]. From the Figure 1a–c XRD diffraction pattern, all three hydrogenated compositions showed a clear peak shift towards a lower 2θ value, indicating BCC lattice expansion due to effective absorption of a significant amount of hydrogen.

Energies **2025**, 18, 3920 9 of 19

No peak shift was observed for the secondary phases. That supports the opinion that this phase could support and/or promote the hydrogen diffusion process at the interface/bulk BCC lattice [79]. It has been experimentally observed in several studies that the typical BCC structure upon hydrogenation shows a phase transformation from BCC to FCC structure [55,56,58–60,80–82]. However, in most cases, an intermediate BCC/BCT monohydride is also formed, which can reversibly store hydrogen up to <1 H/M at moderate temperatures [83,84]. In the present study, for all three compositions, the reaction process developed as follows: BCC + secondary phase ↔ intermediate BCC hydride + secondary phase [22,59,60,81,85,86]. This indicates that upon hydrogenation, the BCC solid solution phase (α -phase) undergoes a phase change to monohydride (β -phase), without converting to dihydride FCC phase (δ), thus establishing an incomplete phase transformation, which can be referred to Figure 1a–c. Few studies have shown that a relatively large presence of a secondary phase reduces the actual storage capacity [34,87]. Long et al. and Silva et al. presented similar lattice expansion of the BCC phase alone up to 50% of hydrogen capacity, as the hydrogen concentration increases, the FCC phase is achieved [38,88]. These results show that for the present compositions, the incomplete phase transformation from BCC to FCC could be due to the presence of a secondary phase, which may hinder hydrogen diffusion at the bulk level, causing a reduction in storage capacity. The alloy may require high pressure (>30 bar) to gain more hydrogen into the lattice, since α - δ phase transformation also depends on the hydrogen concentration [81].

Usually, strong hydride-forming elements (that include Ti, V) have a negative enthalpy of hydride formation value; thus, a higher temperature (~300–400 °C) is required to release hydrogen completely. Efforts to reduce hydride stability have been achieved by adding (non)transition elements, varying the atomic concentrations of constituent elements, and increasing the valence electron concentration (VEC). These are the most effective strategies for destabilizing hydrides in multicomponent systems, including high-entropy alloys [14,47,55,60,89]. It can be seen from the kinetic desorption profile (Figure 3d–f) that not all absorbed hydrogen is released at room temperature. This partial hydrogen release could be due to the contribution from intermetallic phases and/or hydrogen release from the intermediate BCC hydride phase, which typically occurs at a low equilibrium pressure [56,87]. In this study, the addition of Ni and Nb to the TiVCr matrix improved the kinetics performance during absorption and desorption. However, complete desorption was not achieved and requires a temperature of up to 450 °C to release hydrogen from all three compositions, as observed in the TPD results of Figure 1d. Similarly, desorption onset temperature in the range 400–500 °C is also observed in the literature and requires a high temperature for the complete desorption process, which is one of the main challenges in BCC-structured materials [77,87].

3.4. Kinetic Modeling

Kinetic modeling was performed to understand the hydrogen absorption and desorption properties of all three compositions. The time-dependent reaction fraction α (t) is calculated using the definition α (t) = $(P_0 - P_t/P_0 - P_e)$, where P_0 is the initial pressure of the system, and P_t and P_e are the pressures at time t and the final equilibrium pressure. Figure 4a–c shows the reacted fraction (α) of the hydrogen absorption process for all three compositions at different temperatures [47,73,89,90]. All the compositions presented different reaction fraction durations at higher temperatures and showed a saturation time above 600 s to reach 90% of the total absorption capacity. At room temperature, the time taken to reach 90% of the total capacity was t = 1000 s, 2000 s, and 680 s for (TiVCr)₉₅Ni₅, (TiVCr)₉₀Ni₁₀, and (TiVCr)₉₀Ni₅Nb₅, respectively. Regarding the increase in temperature, the reacted fraction (α), especially for (TiVCr)₉₅Ni₅ and (TiVCr)₉₀Ni₁₀,

Energies **2025**, 18, 3920 10 of 19

reaches 90% of its capacity more quickly but exhibits a reduction in storage capacity. In the case of $(TiVCr)_{90}Ni_5Nb_5$ with respect to an increase in temperature, the reacted fraction (α) takes a slightly longer time to reach 90% saturation, indicating that the rate-controlling step occurs either at the interface or at the bulk level. Figure 4d shows the plot of the reacted fraction versus time at room temperature. The results show a faster hydrogen uptake for $(TiVCr)_{95}Ni_5$ and $(TiVCr)_{90}Ni_{10}$ compositions up to $\alpha=0.7$ –0.8. In contrast, $(TiVCr)_{90}Ni_5Nb_5$ showed a short incubation period (t = 125 s) at room temperature, presenting enhanced hydrogen absorption properties. This composition exhibited a shorter duration to reach maximum capacity (t = 35 min) at room temperature.

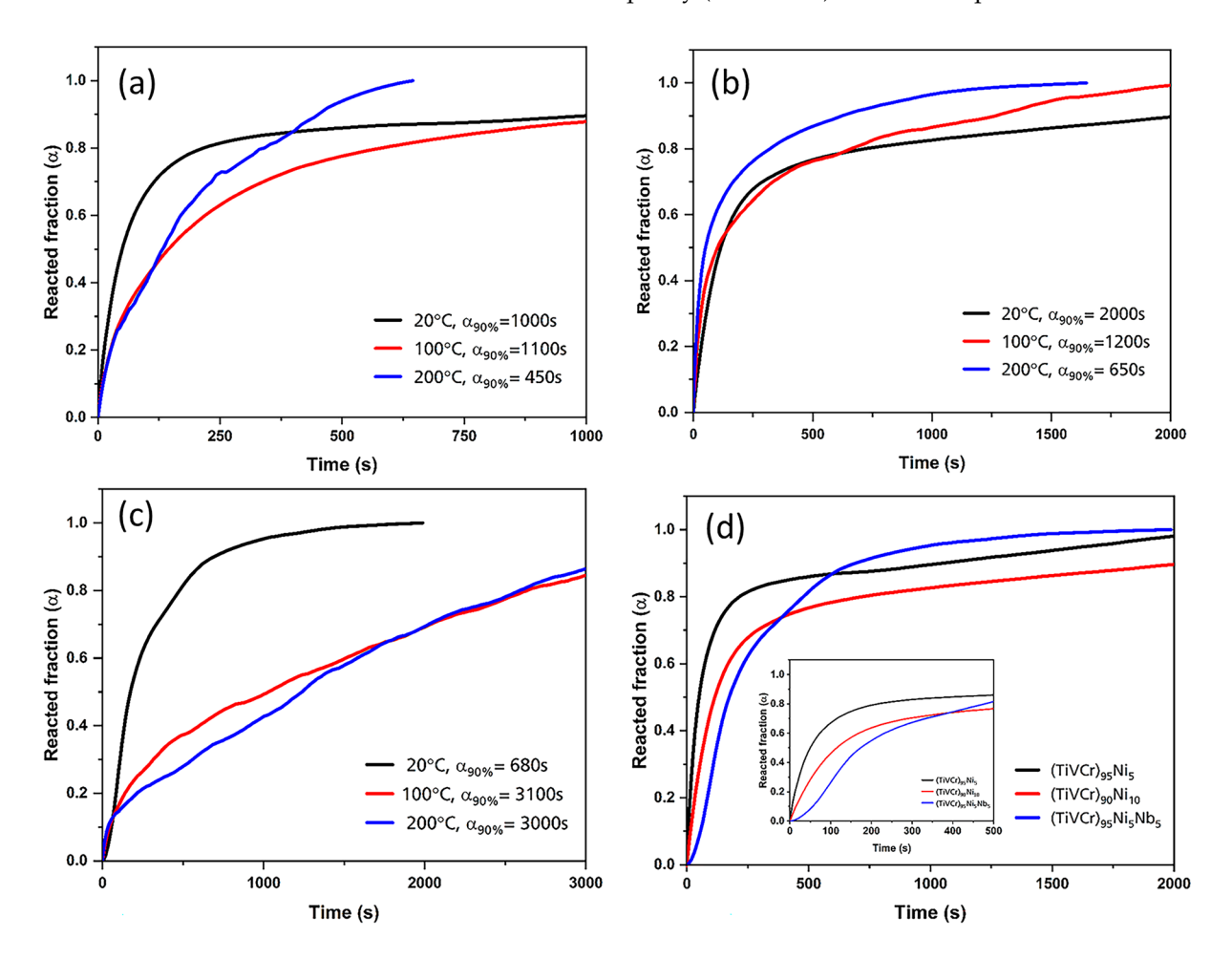


Figure 4. Plots of reacted fraction α vs. t(s) for $(TiVCr)_{95}Ni_5$ (a), $(TiVCr)_{90}Ni_{10}$ (b), and $(TiVCr)_{90}Ni_5Nb_5$ (c) at different temperatures, and (d) reacted fraction at room temperature for comparison.

Hydrogen absorption in metals/alloys depends on the applied pressure and temperature, which drives the reaction [91]. The results of the kinetic modeling at different temperatures for hydrogen absorption are shown in Figure 5. The kinetic data were analyzed using a solid–gas reaction model, and for all three compositions, the Johnson–Mehl–Avrami–Kolmogorov (JMAK) and 3D Jander diffusion models were well-fitted. The results are presented in Figures 5 and 6. The above models are considered the best fit for understanding hydrogen sorption kinetics, as they yielded the highest R² coefficient values, which were closest to 1. The expression for JMAK is $\alpha = 1 - \exp{(-kt)^{\eta}}$, expanding to $\ln{[-\ln{(1-\alpha)}]} = (\eta \ln k) + \eta \ln t$. The 3D diffusion model for Jander is given by equation $[1-(1-\alpha)^{1/3}]^2 = kt$, where α is the reaction fraction at time t, k is the rate constant, and η is the Avrami constant. In general, the hydrogen absorption process proceeds as follows:

Energies **2025**, 18, 3920 11 of 19

(i) physisorption of hydrogen molecules on the surface of the alloy, (ii) dissociation of hydrogen molecules into hydrogen atoms, (iii) penetration of hydrogen into the subsurface layer, (iv) nucleation and growth, and (v) diffusion of hydrogen into the bulk [92]. The development of the entire hydrogen absorption and desorption process over time provides critical insights into the nature of nucleation and growth mechanisms, as well as rate-controlling steps (RCS), at both interface and bulk levels, which can be interpreted using kinetic modeling.

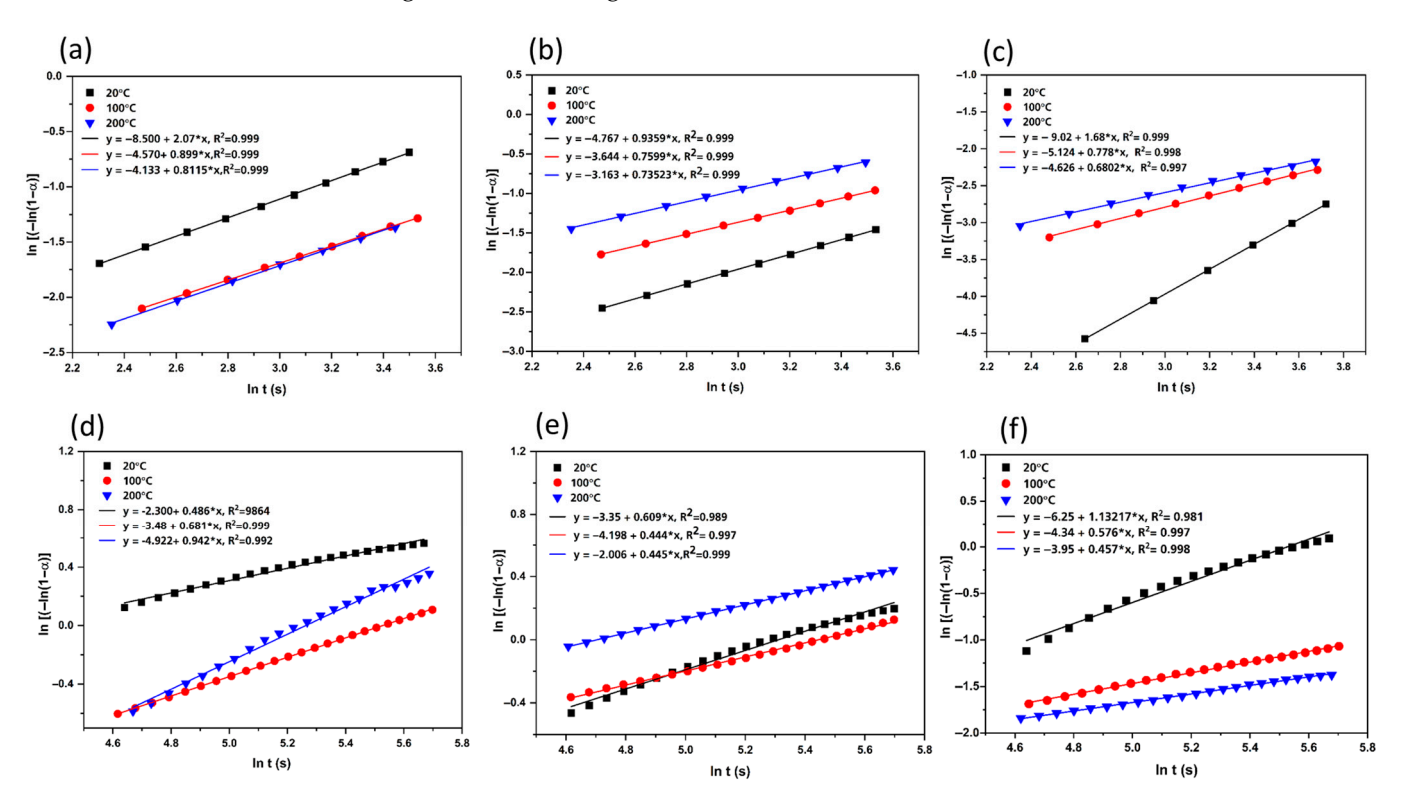


Figure 5. Plots of $\ln(-\ln(1-\alpha))$ vs. $\ln(t)$ of hydrogen absorption kinetics calculated at two different time zones of t = 10–35 s (**a**–**c**) and t = 100–300 s (**d**–**f**) for (TiVCr)₉₅Ni₅ (**a**,**d**), (TiVCr)₉₀Ni₁₀ (**b**,**e**), and (TiVCr)₉₀Ni₅Nb₅ measured at different temperatures (20, 100, and 200 °C).

Figure 5a–f and Table 4 show the calculated values for the Avrami constant (η) and rate constant (k) values at different temperatures for all the three compositions. The nucleation rate for all three compositions for a time period till 300 s shows η = 1–2, showing a 1D interface/diffusion-controlled reaction with a reduced nucleation rate with respect to an increase in temperature [59,93]. Ideally, a high nucleation rate and rapid growth of the hydride phase are essential for a faster hydrogen absorption process. However, several experimental studies have shown that the formation of a hydride layer hinders the hydrogen diffusion process inside the bulk of the alloy. This constitutes a rate-controlling step for the alloy to hydrogenate completely, which is typically seen as a flat curve during kinetic measurements (refer to Figure 2) [89,91,94].

The $(TiVCr)_{95}Ni_5$ and $(TiVCr)_{90}Ni_5Nb_5$ compositions exhibited a decrease in the rate constant with increasing temperature. Both compositions at room temperature showed a higher rate constant (k) value in the time zone (t = 0–35 s) with an Avrami component value (η) of ~2. For time (t = 100–300 s), a gradual decrease in the η and k values was observed for both compositions. This indicates that the kinetics at the interface are faster initially and slow down over time, which is attributed to the rate-controlling step due to hydride shell formation [73]. The decrease in the rate constant value with increasing temperature is due to the exothermic process, where both hydrogenation and dehydrogenation reactions

Energies 2025, 18, 3920 12 of 19

compete with each other, resulting in a decrease in storage capacity at high temperatures. In the case of $(TiVCr)_{90}Ni_{10}$, the rate constant (k) value is found to increase, with an increase in temperature, from 0.0061 to 0.0135 during the time period (t = 0–35 s). The increase in rate during the initial step demonstrates the alloy's ability to quickly absorb hydrogen at the interface level, which may be attributed to an increase in the phase fraction of the secondary phase. Nickel acts as a hydrogen accumulator region, supporting the dissociation of hydrogen.

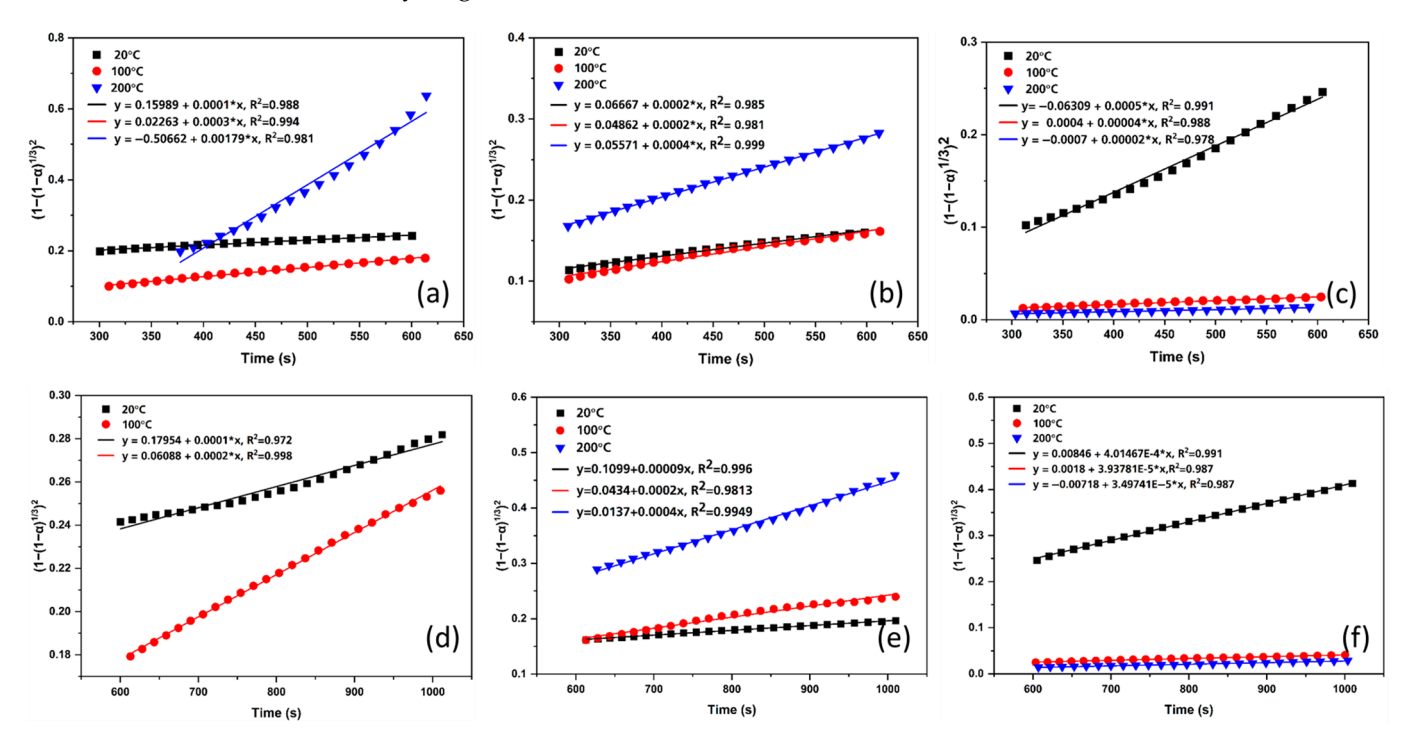


Figure 6. Three-dimensional Jander diffusion model fitting for $(\text{TiVCr})_{95}\text{Ni}_5$ (a), $(\text{TiVCr})_{90}\text{Ni}_{10}$ (b), and $(\text{TiVCr})_{90}\text{Ni}_5\text{Nb}_5$ (c) at different temperatures (20, 100, and 200 °C) for time duration t = 300–600 s and 600–1000 s (**d**–**f**).

Table 4. Results of JMAK at two time stages: 1 (t = 10–35 s) and 2 (t = 100–300 s), η is the Avrami component, k is the rate constant (s).

Composition	Temperature (K)	St	age 1 (t = 0-35	s)	Stage 2 (t = 100–300 s)		
		η	k	\mathbb{R}^2	η	k	\mathbb{R}^2
(TiVCr) ₉₅ Ni ₅	293	2.07	0.0166	0.997	0.486	0.0088	0.986
	373	0.899	0.0062	0.998	0.681	0.0059	0.999
	473	0.811	0.0061	0.999	0.940	0.0053	0.996
(TiVCr) ₉₀ Ni ₁₀	293	0.935	0.0061	0.999	0.609	0.0040	0.989
	373	0.759	0.0082	0.999	0.444	0.00431	0.997
	473	0.735	0.0135	0.999	0.445	0.011	0.999
(TiVCr) ₉₀ Ni ₅ Nb ₅	293	1.684	0.00472	0.999	1.132	0.00397	0.981
	373	0.778	0.00138	0.999	0.576	0.00053	0.997
	473	0.680	0.0011	0.997	0.457	0.00017	0.998

It is generally noted that the reaction rate constant (k) depends on the temperature, which drives the (de)hydrogenation reaction speed. In the present case, the reaction rate (k) decreased with increasing temperature for $(TiVCr)_{95}Ni_5$ and $(TiVCr)_{90}Ni_5Nb_5$, showing a negative temperature dependence. Similar results on the decrease in the rate constant with increasing temperature have been experimentally shown in the literature [95–97],

Energies **2025**, 18, 3920 13 of 19

which indicates that this effect is due to the competition between hydrogen absorption and desorption (exothermic process). Although the goodness of fit is achieved, the JMAK model does not provide an in-depth understanding of the negative temperature effect. All the as-synthesized alloys can absorb hydrogen at room temperature and gradually lose this ability when the temperature increases.

It is generally observed that hydrogen diffusion gradually decreases over time during the hydrogen absorption process, causing a rate-limiting step at the bulk level. Figure 6a-f shows the results of the 3D Jander diffusion model for (TiVCr)₉₅Ni₅, (TiVCr)₉₀Ni₁₀, and (TiVCr)₉₀Ni₅Nb₅ compositions. The diffusion behavior was investigated for two different time ranges, t = 300-600 s, and 600-1000 s, to understand the diffusion limitations over time. The rate constant (k) values for (TiVCr)95Ni5, during the time period (t = 300-600 s), at 20 °C, 100 °C, and 200 °C are 0.0001, 0.0003, and 0.0018, respectively. The k value decreases slightly from 1×10^{-4} to 2×10^{-4} (t ≥ 600 s), with an increase in temperature, which is attributed to a diffusion-controlled step at the bulk level over time due to hydride layer formation. In case of (TiVCr)₉₀Ni₁₀ the k value increases from 0.000136 to 0.0004 for time (t = 300-600 s), and the k value above 600 s decreases from 9×10^{-5} to 4×10^{-5} at increasing temperature (20, 100, and 200 °C). For (TiVCr)₉₀Ni₅Nb₅ at room temperature, the k value for the time period (t = 300–600 s and 600–1000 s) is equal to 0.00050 and 0.0004. This value is slightly higher than that of the other compositions. For temperatures of 100 °C and 200 °C, at a time zone between 300 and 1000 s, the k value is $\sim 3-4 \times 10^{-5}$. This suggests that diffusion is the rate-controlling step as temperature increases, which is also evident from Figures 2 and 4 showing slower hydrogenation reaction performances at 100 °C and 200 °C, whereas at room temperature, (TiVCr)₉₀Ni₅Nb₅ showed enhanced hydrogen diffusion properties.

Figure 7a-c presents the results for the diffusion-controlled mechanism for the hydrogen desorption process for (TiVCr)95Ni5, (TiVCr)90Ni10, and (TiVCr)90Ni5Nb5 compositions at different temperatures. The activation energies for the desorption process were 6.714, 6.135, and 0.436 kJ/mol for (TiVCr)₉₅Ni₅, (TiVCr)₉₀Ni₁₀, and (TiVCr)₉₀Ni₅Nb₅. The desorption of hydrogen for all compositions was promising, with a minimum activation energy. The (TiVCr)₉₀Ni₅Nb₅ composition presented a minimum activation energy for hydrogen release, thus indicating that the addition of Nb not only improved hydrogen diffusion at the bulk level but also destabilized the stability of the alloy-hydrogen interaction(s). Cheng et al. studied the hydrogenation properties of TiVCrNbNi alloys with different Ni concentrations (range 2–6 wt%). The hydrogen desorption activation energy gradually decreased with increasing Ni concentration ($E_a = 93-24 \text{ kJ/mol}$) [98]. In the present work, the lower activation energy for hydrogen desorption may be attributed to the presence of secondary phases, which effectively facilitate hydrogen release at room temperature. These results agree well with the temperature-programmed desorption (TPD) profile, where hydrogen release begins at and above room temperature, and remaining hydrogen can be released only above 300 °C. Typically, strong hydride-forming elements (including Ti and V) have a high enthalpy of hydride formation, requiring high temperatures to release hydrogen completely. The presence of secondary phases supports hydrogen dissociation and enhances the absorption and desorption processes at room temperature. Figure 7d-f can be compared with the desorption curves in Figure 2d-f, where the total dehydrogenation time is shorter for the Nb-substituted alloy, indicating a decrease in the stability of the hydride. Energies **2025**, 18, 3920 14 of 19

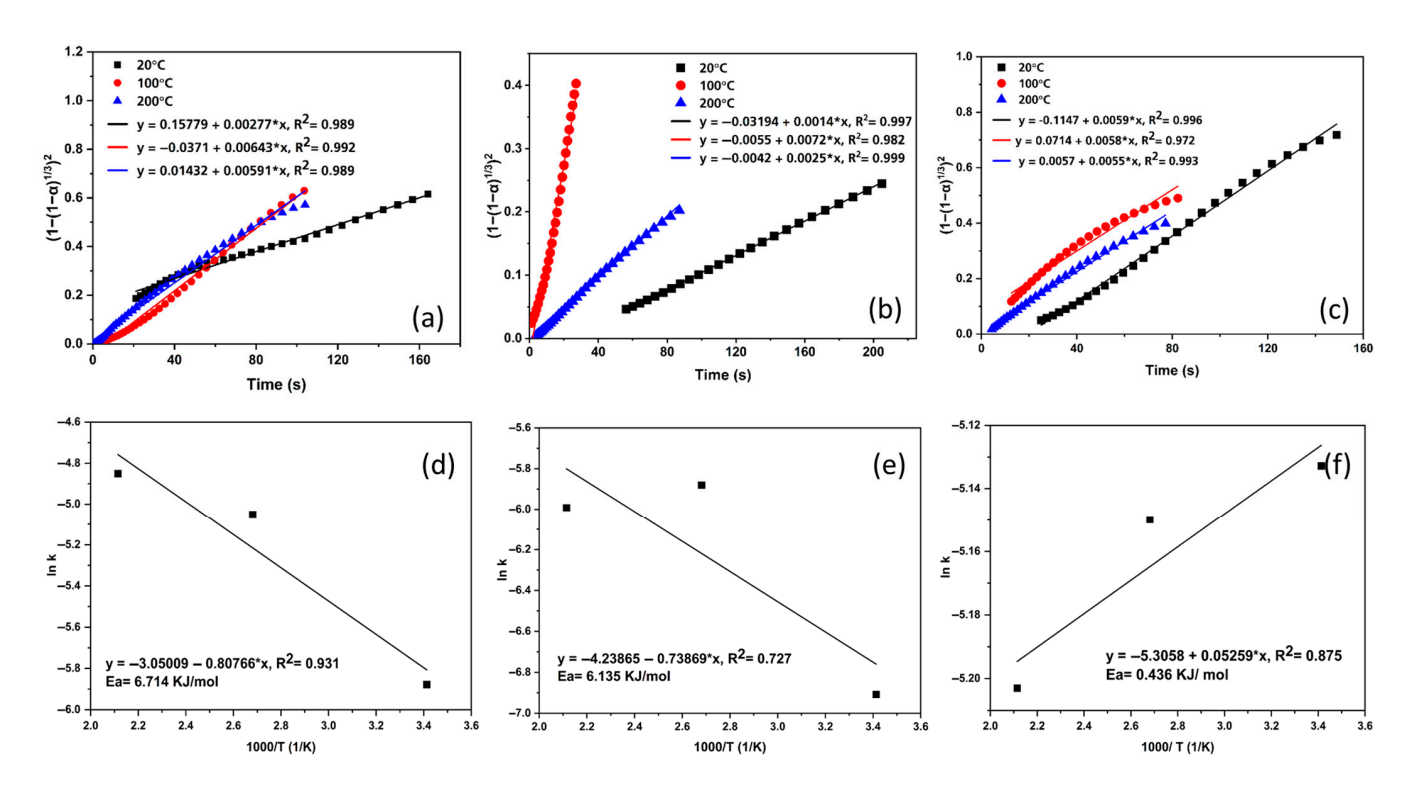


Figure 7. Three-dimensional Jander diffusion model fitting for $(\text{TiVCr})_{95}\text{Ni}_5$ (**a**), $(\text{TiVCr})_{90}\text{Ni}_{10}$ (**b**), and $(\text{TiVCr})_{90}\text{Ni}_5\text{Nb}_5$ (**c**) at different temperatures (20, 100, and 200 °C) and apparent activation energy (E_a) for hydrogen desorption (**d**–**f**).

In summary, the addition of Ni and Nb to the TiVCr and TiVCrNiNb compositions impacted the overall kinetic performance. Specifically, the addition of 5 wt% nickel to $(\text{TiVCr})_{95}\text{Ni}_5$ resulted in 2.5 wt% hydrogen absorption. The kinetic modeling results show enhanced hydrogen absorption at the surface level and improved hydrogen diffusion behavior at the bulk level. In the case of $(\text{TiVCr})_{90}\text{Ni}_{10}$, a hydrogen storage capacity of up to 3 wt% was achieved. The results obtained from kinetic modeling revealed a rate-limiting step at both the interface and bulk levels as time increases. In the case of $(\text{TiVCr})_{90}\text{Ni}_5\text{Nb}_5$, the addition of Nb greatly benefits the hydrogen absorption and desorption processes, resulting in an increase in the rate constant (k) value over time at room temperature, thereby enhancing the overall kinetic performance. In conclusion, Nickel concentration (5 wt%) and Niobium addition facilitated hydrogen absorption and release at room temperature.

4. Conclusions

TiVCr-based alloys are well-explored BCC solid-solution materials for hydrogen storage applications. Improving the kinetic and thermodynamic properties can be achieved by adding (non)transition elements, selecting suitable catalysts, and adjusting the constituent elemental composition. These are the most commonly accepted strategies for enhancing (de)hydrogenation performance. In this study, three compositions, (TiVCr) $_{95}$ Ni $_{5}$, (TiVCr) $_{90}$ Ni $_{10}$, and (TiVCr) $_{90}$ Ni $_{5}$ Nb $_{5}$, were prepared using the arc-melting technique. The hydrogenation properties were studied using kinetic measurements at different temperatures. This study aims to enhance the kinetic absorption step by adding Ni and to improve the hydrogen desorption properties by Nb substitution. Microstructural analysis revealed the presence of a dual phase (BCC + secondary) in all three compositions. The BCC structure actively absorbed hydrogen, and the presence of the secondary phase supported the hydrogen sorption process by dissociating hydrogen at the interface and improving the hydrogen diffusion behavior at the bulk level.

Energies **2025**, 18, 3920 15 of 19

The kinetic modeling results showed that Ni addition increased the nucleation rate at the interface level, and Nb substitution improved the diffusion properties at the bulk level. The apparent activation energies during the desorption process were calculated using the 3D diffusion Jander model, and the values were found to be 6.714, 6.135, and 0.436 kJ/mol for (TiVCr) $_{95}$ Ni $_{5}$, (TiVCr) $_{90}$ Ni $_{10}$, and (TiVCr) $_{90}$ Ni $_{5}$ Nb $_{5}$, respectively. Thus, the inclusion of Nb in TiVCrNi improved bulk-level hydrogen diffusion and facilitated hydrogen desorption at room temperature with a lower activation energy. (TiVCr) $_{95}$ Ni $_{5}$ and (TiVCr) $_{90}$ Ni $_{10}$ exhibited enhanced hydrogen absorption properties. However, higher temperatures above 300 °C are required for complete hydrogen desorption. In this study, the influence of Ni and Nb substitution in Ti-V-Cr-based high-entropy alloys for room-temperature hydrogen storage applications was investigated. The results show that the dual phases improve the overall hydrogen absorption-desorption kinetic properties.

Author Contributions: Conceptualization, T.G.M., D.L.D. and P.H.L.N.; methodology, S.J.; software, S.J. and D.L.D.; validation, S.J., D.L.D. and T.G.M.; formal analysis, S.J. and V.V.R.; investigation, S.J., U.B.R.R., V.V.R., D.L.D. and T.G.M.; resources, S.J.; data curation, S.J., D.L.D. and V.V.R.; writing—original draft preparation, S.J.; writing—review and editing, T.G.M., U.B.R.R., D.L.D. and P.H.L.N.; visualization, S.J. and T.G.M.; supervision, T.G.M.; project administration, T.G.M. All authors have read and agreed to the published version of the manuscript.

Funding: This research received no external funding.

Data Availability Statement: The original contributions presented in this study are included in the article. Further inquiries can be directed to the corresponding author(s).

Conflicts of Interest: Authors Dmitri L. Danilov and Peter H. L. Notten was employed by the company Forschungszentrum Jülich. The remaining authors declare that the research was conducted in the absence of any commercial or financial relationships that could be construed as a potential conflict of interest.

References

- 1. Zivar, D.; Kumar, S.; Foroozesh, J. Underground hydrogen storage: A comprehensive review. *Int. J. Hydrogen Energy* **2021**, 46, 23436–23462. [CrossRef]
- 2. Møller, K.T.; Jensen, T.R.; Akiba, E.; Li, H. Hydrogen—A sustainable energy carrier. *Prog. Nat. Sci. Mater. Int.* **2017**, 27, 34–40. [CrossRef]
- 3. Ishaq, H.; Dincer, I.; Crawford, C. A review on hydrogen production and utilization: Challenges and opportunities. *Int. J. Hydrogen Energy* **2022**, *47*, 26238–26264. [CrossRef]
- Krishnan, A.; Yoosuf, M.; Archana, K.; Arsha, A.S.; Viswam, A. Metal derivative (MD)/g-C₃N₄ association in hydrogen production: A study on the fascinating chemistry behind, current trend & future direction. *J. Energy Chem.* 2023, 80, 562–583. [CrossRef]
- 5. Shanmugasundaram, S.; Thangaraja, J.; Rajkumar, S.; Denis Ashok, S.; Sivaramakrishna, A.; Shamim, T. A review on green hydrogen production pathways and optimization techniques. *Process Saf. Environ. Prot.* **2025**, *197*, 107070. [CrossRef]
- 6. Usman, M.R. Hydrogen storage methods: Review and current status. Renew. Sustain. Energy Rev. 2022, 167, 112743. [CrossRef]
- 7. Sakintuna, B.; Lamari-Darkrim, F.; Hirscher, M. Metal hydride materials for solid hydrogen storage: A review. *Int. J. Hydrogen Energy* **2007**, 32, 1121–1140. [CrossRef]
- 8. Qureshi, T.; Khan, M.M.; Pali, H.S. The future of hydrogen economy: Role of high entropy alloys in hydrogen storage. *J. Alloys Compd.* **2024**, *1004*, *175668*. [CrossRef]
- 9. Yadav, T.P.; Kumar, A.; Verma, S.K.; Mukhopadhyay, N.K. High-Entropy Alloys for Solid Hydrogen Storage: Potentials and Prospects. *Trans. Indian Natl. Acad. Eng.* **2022**, *7*, 147–156. [CrossRef] [PubMed]
- 10. Miracle, D.B.; Senkov, O.N. A critical review of high entropy alloys and related concepts. *Acta Mater.* **2017**, 122, 448–511. [CrossRef]
- 11. Krishna, S.A.; Noble, N.; Radhika, N.; Saleh, B. A comprehensive review on advances in high entropy alloys: Fabrication and surface modification methods, properties, applications, and future prospects. *J. Manuf. Process.* **2024**, *109*, 583–606. [CrossRef]
- 12. Jeyaraman, S.; Manivasagam, T.G. Highly reversible Mg-containing multicomponent high-entropy alloys for electrochemical hydrogen storage applications. *Int. J. Hydrogen Energy* **2024**, *83*, 188–197. [CrossRef]

Energies **2025**, 18, 3920 16 of 19

13. Strozi, R.B.; Leiva, D.R.; Huot, J.; Botta, W.J.; Zepon, G. An approach to design single BCC Mg-containing high entropy alloys for hydrogen storage applications. *Int. J. Hydrogen Energy* **2021**, *46*, 25555–25561. [CrossRef]

- 14. Nygård, M.M.; Ek, G.; Karlsson, D.; Sørby, M.H.; Sahlberg, M.; Hauback, B.C. Counting electrons—A new approach to tailor the hydrogen sorption properties of high-entropy alloys. *Acta Mater.* **2019**, *175*, 121–129. [CrossRef]
- 15. Ek, G.; Nygård, M.M.; Pavan, A.F.; Montero, J.; Henry, P.F.; Sørby, M.H.; Witman, M.; Stavila, V.; Zlotea, C.; Hauback, B.C.; et al. Elucidating the Effects of the Composition on Hydrogen Sorption in TiVZrNbHf-Based High-Entropy Alloys. *Inorg. Chem.* **2021**, 60, 1124–1132. [CrossRef] [PubMed]
- 16. Manivasagam, T.G.; Iliksu, M.; Danilov, D.L.; Notten, P.H.L. Synthesis and electrochemical properties of binary MgTi and ternary MgTi_X (X = Ni, Si) hydrogen storage alloys. *Int. J. Hydrogen Energy* **2017**, *42*, 23404–23415. [CrossRef]
- 17. Ouyang, L.; Liu, F.; Wang, H.; Liu, J.; Yang, X.S.; Sun, L.; Zhu, M. Magnesium-based hydrogen storage compounds: A review. *J. Alloys Compd.* **2020**, *832*, 154865. [CrossRef]
- 18. Crivello, J.C.; Denys, R.V.; Dornheim, M.; Felderhoff, M.; Grant, D.M.; Huot, J.; Jensen, T.R.; de Jongh, P.; Latroche, M.; Walker, G.S.; et al. Mg-based compounds for hydrogen and energy storage. *Appl. Phys. A Mater. Sci. Process.* **2016**, 122, 85. [CrossRef]
- 19. Kohno, T.; Yoshida, H.; Kawashima, F.; Inaba, T.; Sakai, I.; Yamamoto, M.; Kanda, M. Hydrogen storage properties of new ternary system alloys: La₂MgNi₉, La₅Mg₂Ni₂₃, La₃MgNi₁₄. *J. Alloys Compd.* **2000**, *311*, 5–7. [CrossRef]
- 20. Liu, J.; Zhu, S.; Zheng, Z.; Cheng, H.; Yan, K.; Zhu, Z. Long-term hydrogen absorption/desorption properties and structural changes of LaNi₄Co alloy with double desorption plateaus. *J. Alloys Compd.* **2019**, 778, 681–690. [CrossRef]
- 21. Balcerzak, M. Structure and hydrogen storage properties of mechanically alloyed Ti-V alloys. *Int. J. Hydrogen Energy* **2017**, 42, 23698–23707. [CrossRef]
- 22. Shen, S.; Li, Y.; Ouyang, L.; Zhang, L.; Zhu, M.; Liu, Z. V–Ti-Based Solid Solution Alloys for Solid-State Hydrogen Storage. *Nano-Micro Lett.* **2025**, *17*, 175. [CrossRef] [PubMed]
- 23. Kumar, S.; Singh, P.K.; Kojima, Y.; Kain, V. Cyclic hydrogen storage properties of V–Ti–Cr–Al alloy. *Int. J. Hydrogen Energy* **2018**, 43, 7096–7101. [CrossRef]
- 24. Kamble, A.; Sharma, P.; Huot, J. Effect of addition of Zr, Ni, and Zr-Ni alloy on the hydrogen absorption of Body Centred Cubic 52Ti-12V-36Cr alloy. *Int. J. Hydrogen Energy* **2018**, *43*, 7424–7429. [CrossRef]
- 25. Montero, J.; Ek, G.; Laversenne, L.; Nassif, V.; Zepon, G.; Sahlberg, M.; Zlotea, C. Hydrogen storage properties of the refractory Ti–V–Zr–Nb–Ta multi-principal element alloy. *J. Alloys Compd.* **2020**, *835*, 155376. [CrossRef]
- 26. Ma, X.F.; Ding, X.; Liu, E.L.; Chen, R.R.; Wang, X.X.; Zhang, Y.; Guo, J.J. Modification of BCC phase and the enhanced reversible hydrogen storage properties of Ti-V-Fe-Mn alloys with varied V/Fe ratios. *China Foundry* **2024**, *21*, 546–554. [CrossRef]
- 27. Matsunaga, T.; Kon, M.; Washio, K.; Shinozawa, T.; Ishikiriyama, M. TiCrVMo alloys with high dissociation pressure for high-pressure MH tank. *Int. J. Hydrogen Energy* **2009**, *34*, 1458–1462. [CrossRef]
- 28. Yu, X.; Wu, Z.; Xia, B.; Xu, N. Enhancement of hydrogen storage capacity of Ti–V–Cr–Mn BCC phase alloys. *J. Alloys Compd.* **2004**, 372, 272–277. [CrossRef]
- 29. Zareipour, F.; Shahmir, H.; Huang, Y.; Patel, A.K.; Dematteis, E.M.; Baricco, M. Hydrogen storage in TiVCr(Fe,Co)(Zr,Ta) multi-phase high-entropy alloys. *Int. J. Hydrogen Energy* **2024**, *94*, 639–649. [CrossRef]
- 30. Towata, S.I.; Noritake, T.; Itoh, A.; Aoki, M.; Miwa, K. Cycle durability of Ti-Cr-V alloys partially substituted by Nb or Fe. *J. Alloys Compd.* **2013**, *580* (Suppl. S1), S226–S228. [CrossRef]
- 31. Wu, Y.; Zhao, W.; Jiang, L.; Li, Z.; Guo, X.; Ye, J.; Yuan, B.; Wang, S.; Hao, L. Effect of Fe and Al on hydrogen storage properties of 75 V-Ti-Cr alloys. *J. Alloys Compd.* **2021**, *887*, 161181. [CrossRef]
- 32. Coluzzi, B.; Biscarini, A.; Mazzolai, G.; Mazzolai, F.M.; Tuissi, A.; Agresti, F.; Lo Russo, S.; Maddalena, A.; Palade, P.; Principi, G. Physical properties of hydrogen in TiVMnCr bcc alloys as deduced from hydrogen absorption/desorption and mechanical spectroscopy experiments. *J. Alloys Compd.* 2008, 456, 118–124. [CrossRef]
- 33. Montero, J.; Zlotea, C.; Ek, G.; Crivello, J.C.; Laversenne, L.; Sahlberg, M. TiVZrNb Multi-Principal-Element Alloy: Synthesis Optimization, Structural, and Hydrogen Sorption Properties. *Molecules* **2019**, 24, 2799. [CrossRef] [PubMed]
- 34. Liu, J.; Xu, J.; Sleiman, S.; Chen, X.; Zhu, S.; Cheng, H.; Huot, J. Microstructure and hydrogen storage properties of Ti–V–Cr based BCC-type high entropy alloys. *Int. J. Hydrogen Energy* **2021**, *46*, 28709–28718. [CrossRef]
- 35. Liu, H.; Zhang, J.; Sun, P.; Zhou, C.; Liu, Y.; Fang, Z.Z. An overview of TiFe alloys for hydrogen storage: Structure, processes, properties, and applications. *J. Energy Storage* **2023**, *68*, 107772. [CrossRef]
- 36. Sato, T.; Saitoh, H.; Utsumi, R.; Ito, J.; Nakahira, Y.; Obana, K.; Takagi, S.; Orimo, S.I. Hydrogen Absorption Reactions of Hydrogen Storage Alloy LaNi₅ under High Pressure. *Molecules* **2023**, *28*, 1256. [CrossRef] [PubMed]
- 37. Balcerzak, M.; Wagstaffe, M.; Robles, R.; Pruneda, M.; Noei, H. Effect of Cr on the hydrogen storage and electronic properties of BCC alloys: Experimental and first-principles study. *Int. J. Hydrogen Energy* **2020**, *45*, 28996–29008. [CrossRef]
- 38. Silva, B.H.; Zlotea, C.; Vaughan, G.; Champion, Y.; Botta, W.J.; Zepon, G. Hydrogen absorption/desorption reactions of the (TiVNb)₈₅Cr₁₅ multicomponent alloy. *J. Alloys Compd.* **2022**, *901*, 163620. [CrossRef]

Energies **2025**, 18, 3920 17 of 19

39. Mazzolai, G.; Coluzzi, B.; Biscarini, A.; Mazzolai, F.M.; Tuissi, A.; Agresti, F.; Lo Russo, S.; Maddalena, A.; Palade, P.; Principi, G. Hydrogen-storage capacities and H diffusion in bcc TiVCr alloys. *J. Alloys Compd.* **2008**, 466, 133–139. [CrossRef]

- 40. Arashima, H.; Takahashi, F.; Ebisawa, T.; Itoh, H.; Kabutomori, T. Correlation between hydrogen absorption properties and homogeneity of Ti-Cr-V alloys. *J. Alloys Compd.* **2003**, 356–357, 405–408. [CrossRef]
- 41. Feng, Z.; Zhong, H.; Li, D.; Li, X.; Yang, B.; Li, S. Microstructure and hydrogen storage properties of Ti–V–Mn alloy with Zr, Ni, and Zr₇Ni₁₀ addition. *J. Mater. Res.* **2022**, *37*, 1591–1601. [CrossRef]
- 42. Pericoli, E.; Ferretti, V.; Verna, D.; Pasquini, L. Tuning TiFe_{1-x}Ni_x Hydride Thermodynamics through Compositional Tailoring. *ACS Appl. Energy Mater.* **2025**, *8*, 2135–2144. [CrossRef] [PubMed]
- 43. Dematteis, E.M.; Berti, N.; Cuevas, F.; Latroche, M.; Baricco, M. Substitutional effects in TiFe for hydrogen storage: A comprehensive review. *Mater. Adv.* **2021**, *2*, 2524–2560. [CrossRef]
- 44. Soleimani, A.; Hosseini Dolatabadi, S.H.; Heidari, M.; Pinnarelli, A.; Mehdizadeh Khorrami, B.; Luo, Y.; Vizza, P.; Brusco, G. Progress in hydrogen fuel cell vehicles and up-and-coming technologies for eco-friendly transportation: An international assessment. *Multiscale Multidiscip. Model. Exp. Des.* 2024, 7, 3153–3172. [CrossRef]
- 45. U.S. Department of Energy. *Target Explanation Document: Onboard Hydrogen Storage for Light-Duty Fuel Cell Vehicles*; U.S. Drive, U.S. Department of Energy: Washington, DC, USA, 2017; pp. 1–29. Available online: https://www.energy.gov/sites/prod/files/2015/05/f22/fcto_myrdd_storage.pdf (accessed on 10 January 2025).
- Cho, S.W.; Han, C.S.; Park, C.N.; Akiba, E. Hydrogen storage characteristics of Ti-Cr-V alloys. *J. Alloys Compd.* 1999, 288, 294–298.
 [CrossRef]
- 47. Kumar, A.; Banerjee, S.; Pillai, C.G.S.; Bharadwaj, S.R. Hydrogen storage properties of Ti_{2-x}CrVM_x (M = Fe, Co, Ni) alloys. *Int. J. Hydrogen Energy* **2013**, *38*, 13335–13342. [CrossRef]
- 48. Kumar, A.; Banerjee, S.; Ruz, P.; Sudarsan, V. Hydrogen storage properties of Al-containing Ti₂CrV alloys. *Bull. Mater. Sci.* **2024**, 47, 8. [CrossRef]
- Kumar, A.; Shashikala, K.; Banerjee, S.; Nuwad, J.; Das, P.; Pillai, C.G.S. Effect of cycling on hydrogen storage properties of Ti₂CrV alloy. *Int. J. Hydrogen Energy* 2012, 37, 3677–3682. [CrossRef]
- 50. Kumar, A.; Banerjee, S.; Bharadwaj, S.R. Hydrogen storage properties of Ti_{0.32}Cr_{0.43}V_{0.25} alloy and its composite with TiMn₂. J. Alloys Compd. **2015**, 649, 801–808. [CrossRef]
- 51. Singh, B.K.; Cho, S.W.; Bartwal, K.S. Effect on structure and hydrogen storage characteristics of composite alloys Ti_{0.32}Cr_{0.43}V_{0.25} with LaNi₅ and rare-earth elements La, Ce, Y.J. *Alloys Compd.* **2009**, *478*, 785–788. [CrossRef]
- 52. Banerjee, S.; Kumar, A.; Ruz, P.; Sengupta, P. Influence of Laves phase on microstructure and hydrogen storage properties of Ti–Cr–V based alloy. *Int. J. Hydrogen Energy* **2016**, *41*, 18130–18140. [CrossRef]
- 53. Akiba, E.; Iba, H. Hydrogen absorption by Laves phase related BCC solid solution. *Intermetallics* 1998, 6, 461–470. [CrossRef]
- 54. Zhu, Y.; Li, X.; Yang, X.S.; Chen, P.; Tsui, G.C.P.; Xu, Z.L.; Tang, R.; Xiao, F.; Chan, K. Compositionally complex doping for low-V Ti-Cr-V hydrogen storage alloys. *Chem. Eng. J.* **2023**, 477, 146970. [CrossRef]
- 55. Silva, B.H.; Zlotea, C.; Champion, Y.; Botta, W.J.; Zepon, G. Design of TiVNb-(Cr, Ni or Co) multicomponent alloys with the same valence electron concentration for hydrogen storage. *J. Alloys Compd.* **2021**, *865*, 158767. [CrossRef]
- 56. Strozi, R.B.; Silva, B.H.; Leiva, D.R.; Zlotea, C.; Botta, W.J.; Zepon, G. Tuning the hydrogen storage properties of Ti-V-Nb-Cr alloys by controlling the Cr/(TiVNb) ratio. *J. Alloys Compd.* **2023**, 932, 167609. [CrossRef]
- 57. Bishnoi, A.; Sharma, P. Large-scale production of BCC solid solution hydrogen storage alloy. *Int. J. Hydrogen Energy* **2024**, 75, 294–302. [CrossRef]
- 58. Cheng, B.; Li, Y.; Li, X.; Ke, H.; Wang, L.; Cao, T.; Wan, D.; Wang, B.; Xue, Y. Solid-State Hydrogen Storage Properties of Ti–V–Nb–Cr High-Entropy Alloys and the Associated Effects of Transitional Metals (M = Mn, Fe, Ni). *Acta Metall. Sin. Engl. Lett.* **2022**, *36*, 1113–1122. [CrossRef]
- 59. Liang, J.; Li, G.; Ding, X.; Li, Y.; Wen, Z.; Zhang, T.; Qu, Y. The synergistic effect of Ni and C14 Laves phase on the hydrogen storage properties of TiVZrNbNi high entropy hydrogen storage alloy. *Intermetallics* **2024**, *164*, 108102. [CrossRef]
- 60. Chanchetti, L.F.; Hessel Silva, B.; Montero, J.; Zlotea, C.; Champion, Y.; Botta, W.J.; Zepon, G. Structural characterization and hydrogen storage properties of the Ti₃₁V₂₆Nb₂₆Zr₁₂M₅ (M = Fe, Co, or Ni) multi-phase multicomponent alloys. *Int. J. Hydrogen Energy* **2023**, *48*, 2247–2255. [CrossRef]
- 61. Qin, J.; Liu, Z.; Zhao, W.; Wang, D.; Zhang, Y.; Zhong, Y.; Zhang, X.; Wang, Z.; Hu, C.; Liu, J. Hydrogen transportation behaviour of V–Ni solid solution: A first-principles investigation. *Materials* **2021**, *14*, 2603. [CrossRef] [PubMed]
- 62. Yao, J.Y.; de Paula Santos, W.; Moussa, M.; Serrano, L.B.; Bobet, J.L.; Santos, S.F.; Cardoso, K.R. Effect of Nb on hydrogen storage properties of Ti–V–Cr-based alloys. *Mater. Chem. Phys.* **2024**, *328*, 130011. [CrossRef]
- 63. Takeuchi, A.; Akira, A.I. Classification of Bulk Metallic Glasses by Atomic Size Difference, Heat of Mixing and Period of Constituent Elements and Its Application to Characterization of the Main Alloying Element. *Mater. Trans.* 2005, 46, 2817–2829. [CrossRef]

Energies **2025**, *18*, 3920 18 of 19

64. Guo, S.; Liu, C.T. Phase stability in high entropy alloys: Formation of solid-solution phase or amorphous phase. *Prog. Nat. Sci. Mater. Int.* **2011**, *21*, 433–446. [CrossRef]

- 65. Strozi, R.B.; Leiva, D.R.; Huot, J.; Botta, W.J.; Zepon, G. Synthesis and hydrogen storage behavior of Mg–V–Al–Cr–Ni high entropy alloys. *Int. J. Hydrogen Energy* **2021**, *46*, 2351–2361. [CrossRef]
- 66. Griessen, R.; Riesterer, T. Heat of formation models. In *Hydrogen in Intermetallic Compounds I*; Springer: Berlin/Heidelberg, Germany, 1988; pp. 219–284.
- 67. Tominaga, Y.; Matsumoto, K.; Fuda, T.; Tamura, T.; Kuriiwa, T.; Kamegawa, A.; Takamura, H.; Okada, M. Protium absorption desorption properties of Ti-V-Cr-(Mn,Ni) Alloy. *Mater. Trans.* **2000**, *41*, 617–620. [CrossRef]
- 68. Wen, Z.; Li, G.; Wang, S.; Li, Y.; Zhang, T.; Ding, X.; Qu, Y. Effect of C15 Laves phase ratios on hydrogen absorption and desorption properties of $Ti_{0.50-x}V_{0.25}Cr_xNb_{0.25}$ (x = 0.15, 0.25, 0.30, and 0.35) multicomponent alloys. *J. Alloys Compd.* **2025**, 1018, 179159. [CrossRef]
- 69. Kumar, A.; Yadav, T.P.; Mukhopadhyay, N.K. Notable hydrogen storage in Ti–Zr–V–Cr–Ni high entropy alloy. *Int. J. Hydrogen Energy* **2022**, 47, 22893–22900. [CrossRef]
- 70. Gao, M.; Zhang, S.; Miao, H.; Liu, Y.; Pan, H. Pulverization mechanism of the multiphase Ti-V-based hydrogen storage electrode alloy during charge/discharge cycling. *J. Alloys Compd.* **2010**, *489*, 552–557. [CrossRef]
- 71. Luo, L.; Yang, F.; Li, Y.; Li, L.; Li, Y. Investigation of the microstructure and hydrogen storage behavior of $V_{48}Fe_{12}Ti_{15+x}Cr_{25-x}$ (x = 0, 5, 10, 15) alloys. *Int. J. Hydrogen Energy* **2022**, 47, 9653–9671. [CrossRef]
- 72. Aranda, V.; Leiva, D.R.; Huot, J.; Botta, W.J.; Zepon, G. Hydrogen storage properties of the TiVFeZr multicomponent alloy with C14-type laves phase structure. *Intermetallics* **2023**, *162*, 108020. [CrossRef]
- 73. Ma, X.; Ding, X.; Chen, R.; Chen, X.; Song, Q.; Cui, H. Study on microstructure and the hydrogen storage behavior of a TiVZrNbFe high-entropy alloy. *Intermetallics* **2023**, *157*, 107885. [CrossRef]
- 74. Li, G.; Li, Y.; Liang, J.; Wen, Z.; Zhang, T.; Ding, X.; Qu, Y. Influence of C14 Laves phase and Zr-rich phase interactions on the hydrogen storage properties of Ti_{32.5}V_{27.5}Zr_{7.5}Nb_{32.5} high entropy hydrogen storage alloy. *Intermetallics* **2024**, *168*, 108239. [CrossRef]
- 75. Ponsoni, J.B.; Aranda, V.; da Nascimento, T.S.; Strozi, R.B.; Botta, W.J.; Zepon, G. Design of multicomponent alloys with C14 laves phase structure for hydrogen storage assisted by computational thermodynamic. *Acta Mater.* **2022**, 240, 118317. [CrossRef]
- 76. Yartys, V.A.; Lototskyy, M.V. Laves type intermetallic compounds as hydrogen storage materials: A review. *J. Alloys Compd.* **2022**, 916, 165219. [CrossRef]
- 77. Dangwal, S.; Edalati, K. Significance of interphase boundaries on activation of high-entropy alloys for room-temperature hydrogen storage. *Int. J. Hydrogen Energy* **2024**, *50*, 626–636. [CrossRef]
- 78. Floriano, R.; Zepon, G.; Edalati, K.; Fontana, G.L.B.G.; Mohammadi, A.; Ma, Z.; Li, H.W.; Contieri, R.J. Hydrogen storage in TiZrNbFeNi high entropy alloys, designed by thermodynamic calculations. *Int. J. Hydrogen Energy* **2020**, *45*, 33759–33770. [CrossRef]
- 79. Guéguen, A.; Joubert, J.M.; Latroche, M. Influence of the C14 Ti_{35.4}V_{32.3}Fe_{32.3} Laves phase on the hydrogenation properties of the body-centered cubic compound Ti_{24.5}V_{59.3}Fe_{16.2}. *J. Alloys Compd.* **2011**, *509*, 3013–3018. [CrossRef]
- 80. Hessel Silva, B.; Botta, W.J.; Zepon, G. Design of a Ti–V–Nb–Cr alloy with room temperature hydrogen absorption/desorption reversibility. *Int. J. Hydrogen Energy* **2023**, *48*, 32813–32825. [CrossRef]
- 81. Zlotea, C.; Sow, M.A.; Ek, G.; Couzinié, J.P.; Perrière, L.; Guillot, I.; Bourgon, J.; Møller, K.T.; Jensen, T.R.; Akiba, E.; et al. Hydrogen sorption in TiZrNbHfTa high entropy alloy. *J. Alloys Compd.* **2019**, 775, 667–674. [CrossRef]
- 82. Sahlberg, M.; Karlsson, D.; Zlotea, C.; Jansson, U. Superior hydrogen storage in high entropy alloys. *Sci. Rep.* **2016**, *6*, 36770. [CrossRef] [PubMed]
- 83. Bouzidi, A.; Laversenne, L.; Nassif, V.; Elkaim, E.; Zlotea, C. Hydrogen Storage Properties of a New Ti-V-Cr-Zr-Nb High Entropy Alloy. *Hydrogen* **2022**, *3*, 270–284. [CrossRef]
- 84. Cho, S.W.; Yoo, J.H.; Chang, H.K.; Kim, W.B.; Kil, D.S.; Ahn, J.G. Changes in the microstructure and hydrogen storage properties of Ti-Cr-V alloys by ball milling and heat treatment. *J. Alloys Compd.* **2011**, *509*, *5545–5550*. [CrossRef]
- 85. Sleiman, S.; Huot, J. Effect of particle size, pressure and temperature on the activation process of hydrogen absorption in TiVZrHfNb high entropy alloy. *J. Alloys Compd.* **2021**, *861*, 158615. [CrossRef]
- 86. Zhai, Y.T.; Li, Y.M.; Wei, S.H.; Tolj, I.; Kennedy, J.; Yang, F. Progress in V-BCC based solid solution hydrogen storage alloys. J. Energy Storage 2025, 109, 115103. [CrossRef]
- 87. Liu, J.; Xu, J.; Sleiman, S.; Ravalison, F.; Zhu, W.; Liu, H.; Cheng, H.; Huot, J. Hydrogen storage properties of V_{0.3}Ti_{0.3}Cr_{0.25}Mn_{0.1}Nb_{0.05} high entropy alloy. *Int. J. Hydrogen Energy* **2022**, 47, 25724–25732. [CrossRef]
- 88. Luo, L.; Han, H.; Feng, D.; Lv, W.; Chen, L.; Li, L.; Zhai, T.; Liu, S.; Sun, S.; Li, Y.; et al. Nanocrystalline High Entropy Alloys with Ultrafast Kinetics and High Storage Capacity for Large-Scale Room-Temperature-Applicable Hydrogen Storage. *Renewables* 2024, 2, 138–149. [CrossRef]

Energies **2025**, 18, 3920 19 of 19

89. Zhang, J.W.; Zhou, P.P.; Cao, Z.M.; Li, P.C.; Hu, J.T.; Xiao, H.Y.; Zhou, X.S.; Shen, H.H.; Zu, X.T. Composition and temperature influence on hydrogenation performance of TiZrHfMo_xNb_{2-x} high entropy alloys. *J. Mater. Chem. A* **2023**, *11*, 20623–20635. [CrossRef]

- 90. Ma, X.; Ding, X.; Chen, R.; Cao, W.; Song, Q. Study on hydrogen storage property of (ZrTiVFe)_xAly high-entropy alloys by modifying Al content. *Int. J. Hydrogen Energy* **2022**, *47*, 8409–8418. [CrossRef]
- 91. Das, T.K.; Kumar, A.; Ruz, P.; Banerjee, S.; Sudarsan, V. Hydrogen storage properties of Ti2FeV BCC solid solution. *J. Chem. Sci.* **2019**, *131*, 98. [CrossRef]
- 92. Gupta, A.; Baron, G.V.; Perreault, P.; Lenaerts, S.; Ciocarlan, R.G.; Cool, P.; Mileo, P.G.M.; Rogge, S.; Van Speybroeck, V.; Watson, G.; et al. Hydrogen Clathrates: Next Generation Hydrogen Storage Materials. *Energy Storage Mater.* **2021**, *41*, 69–107. [CrossRef]
- 93. Zhang, S.; Ding, X.; Chen, R.; Zhang, J.; Su, Y.; Wu, S.; Guo, J. Modification of nano-eutectic structure and the relation on hydrogen storage properties: A novel Ti–V–Zr medium entropy alloy. *Int. J. Hydrogen Energy* **2022**, *47*, 34533–34544. [CrossRef]
- 94. Ruz, P.; Banerjee, S.; Halder, R.; Kumar, A.; Sudarsan, V. Thermodynamics, kinetics and microstructural evolution of Ti_{0.43}Zr_{0.07}Cr_{0.25}V_{0.25} alloy upon hydrogenation. *Int. J. Hydrogen Energy* **2017**, 42, 11482–11492. [CrossRef]
- 95. Hara, M. Hydrogen-induced disproportionation of Zr₂Co. J. Alloys Compd. 2003, 352, 218–225. [CrossRef]
- 96. Li, J.; Xu, L.; Jiang, X.; Li, X. Study on the hydrogen storage property of $(TiZr_{0.1})_xCr_{1.7-y}FeyMn_{0.3}$ (1.05 < x < 1.2, 0.2 < y < 0.6) alloys. *Prog. Nat. Sci. Mater. Int.* **2018**, 28, 470–477. [CrossRef]
- 97. Li, T.; Li, Q.; Long, H.; Chou, K.C.; Luo, Q. Interpretation of negative temperature dependence of hydriding reaction in LaNi₅-Mg alloys by modified Chou model. *Catal. Today* **2018**, *318*, 97–102. [CrossRef]
- 98. Cheng, B.; Kong, L.; Cai, H.; Li, Y.; Zhao, Y.; Wan, D.; Xue, Y. Exploring microstructure variations and hydrogen storage characteristics in TiVNbCrNi high-entropy alloys with different Ni incorporation. *Int. J. Hydrogen Energy* **2024**, 72, 29–40. [CrossRef]

Disclaimer/Publisher's Note: The statements, opinions and data contained in all publications are solely those of the individual author(s) and contributor(s) and not of MDPI and/or the editor(s). MDPI and/or the editor(s) disclaim responsibility for any injury to people or property resulting from any ideas, methods, instructions or products referred to in the content.